



OPEN

## The role of Faraday effect on the one-dimensional n-doped Si photonic crystals towards magnetic field sensing applications

Hussein A. Elsayed<sup>1</sup>✉, Ashour M. Ahmed<sup>2</sup>, Nazly Samy<sup>3</sup>, Abinash Panda<sup>4</sup>, M. A. Abdelkawy<sup>5</sup>, Hassan Sayed<sup>6</sup>, Mazen M. Abadla<sup>7</sup>, Mohannad Al-Hmoud<sup>2</sup>, Wail Al Zoubi<sup>8</sup> & Ahmed Mehaney<sup>3</sup>

In this study, we have proposed a one-dimensional photonic crystal (1D-PhC) structure for the detection and monitoring of magnetic field intensities. In this regard, the designed magnetic field sensor is introduced to operate in THz frequencies within the wavelength range from 120 μm to 300 μm. The sensing mechanism relies on the Faraday effect, which influences the permittivity of an n-doped silicon that is employed as a defect layer inside the designed PhC structure. Meanwhile, the optimal sensor configuration consists of alternating layers of SiO<sub>2</sub> and GaAs, arranged in the form; (SiO<sub>2</sub> + GaAs)<sup>N=4</sup>/n-doped Si / (SiO<sub>2</sub> + GaAs)<sup>N=4</sup>. Additionally, the numerical simulations are conducted in the vicinity of the transfer matrix method, plasma model and Faraday effect as well. To improve sensor performance, various structural parameters, including the thickness, doping concentration (N<sub>d</sub>) of the n-doped Si layer, the constituent materials of PhC structure, the number of unit cells, and the incident angle as well are optimized. Moreover, the sensor's effectiveness is evaluated based on sensitivity, quality factor (Q-factor), figure of merit (FOM), and detection limit. Upon optimization, the proposed sensor demonstrates a high sensitivity of 2.91 μm/Tesla and a Q-factor of 1600 across a magnetic field range of 1 to 10 Tesla, which proves its ability as a potential magnetic field sensor. Moreover, the designed sensor is robust against structure disorders and geometrical variations as well.

**Keywords** Magnetic field, Photonic crystal, Magnetic field sensor, Defective photonic crystal, Permittivity, Transfer matrix method, Faraday geometry

With the rapid advancement of technology, magnetic field sensors have become integral both directly and indirectly in facilitating global progress. Therefore, it is essential to provide a precise measurement of magnetic fields across a wide range of research areas and practical applications, including industrial manufacturing, medical diagnostics, national defense, and resource exploration<sup>1–4</sup>. In this regard, numerous methods have been introduced for sensing the magnetic field such as Hall Effect, electromagnetic induction, tunnel magnetoresistance, giant magnetoresistance, anisotropic magnetoresistance, magneto-optical effect, nuclear precession, and superconducting quantum interface<sup>2,4,5</sup>. Conventional magnetic field sensing techniques rely on electromagnetic principles to convert magnetic signals into electrical signals. However, these electrically based sensors are suffering from several limitations, including large physical size, high fabrication costs, complex structural designs, integration challenges, susceptibility to electromagnetic interference, and the requirement for temperature control systems. In contrast, sensors based on the magneto-optical effect effectively address these

<sup>1</sup>Department of Physics, College of Science, University of Ha'il, P.O. Box 2440, Ha'il, Saudi Arabia. <sup>2</sup>Physics Department, College of Science, Imam Mohammad Ibn Saud Islamic University (IMSIU), Riyadh 11623, Saudi Arabia. <sup>3</sup>Photonic and phononic crystals Lab, Physics Department, Faculty of Science, Beni-Suef University, Beni-Suef 62512, Egypt. <sup>4</sup>Department of Electronics and Communication Engineering, CMR Institute of Technology, Bengaluru 560037, India. <sup>5</sup>Department of Mathematics and Statistics, College of Science, Imam Mohammad Ibn Saud Islamic University (IMSIU), Riyadh 11423, Saudi Arabia. <sup>6</sup>Physics Department, Faculty of Science, TH-PPM Group, Beni-Suef University, Beni-Suef 62512, Egypt. <sup>7</sup>Physics Department, Faculty of Science, Al-Aqsa University, Palestinian Authority, Gaza City, Palestine. <sup>8</sup>Materials Electrochemistry Laboratory, School of Materials Science and Engineering, Yeungnam University, Gyeongsan 38541, Republic of Korea. ✉email: drhussien85sc@gmail.com; Hu.Abdelghany@uoh.edu.sa

issues, offering significant advantages such as high sensitivity, compatibility with large-area distributed sensing, a broad dynamic range, inherent multiplexing capabilities, and strong adaptability to varying environmental conditions<sup>3,6</sup>.

Magneto-optical effect (MOE) refers to the interaction between electromagnetic waves (EMWs) and material placed in an external of magnetic field. The MOE is categorized into several distinct phenomena, including the Faraday, cotton-Mouton, Voigt, Magneto-Optical Kerr Effect (MOKE)<sup>1,7-9</sup>. These effects are promising to alter the optical properties specifically the permittivity of the material like metals and doped semiconductors<sup>10</sup>. In the last two decades, the Faraday effect emerges as an effective technique for envisaging the sensing applications<sup>1,11,12</sup>. Notably, Faraday geometry provides a significant contribution to tuning the optical characteristics of the dispersive media. In Faraday effect, the direction of the external magnetic field must be parallel to the direction of the propagation of the EMW causing either left or right circular polarization for the eigenmodes. Accordingly, the influence of the Faraday effect has been incorporated into the design of our proposed magnetic field sensor. In contrast, under the Voigt effect, the eigenmodes remain linearly polarized due to the orientation of the external magnetic field being normal to the propagation direction of the electromagnetic wave<sup>10,13</sup>, whereas, in MOKE method, the polarization is elliptical<sup>1</sup>. In recent years, there has been a growing interest in applying magneto-optical effects in periodic structures like photonic crystals (PhCs).

PhCs are artificial designed periodic multilayers structures comprising at least two or more materials of different optical properties in each unit cell<sup>14,15</sup>. The periodicity of PhC structures can be implemented in one (1D), tow (2D), or three-dimensions (3D)<sup>16</sup>. One of the distinguishing characteristics of PhCs is the emergence of photonic band gaps (PBGs), which arises due to Bragg scattering of incident waves at the interfaces between different layers of the designed structure. PBGs are defined as bands of frequencies in which the propagation of the EMWs of similar frequencies is prohibited<sup>17</sup>. Therefore, this unique property allows for PhCs to control the propagation of the incident EMWs<sup>17,18</sup>. Consequently, the PBG has enabled a wide range of applications for PhCs, such as optical isolators, optical fibers, and integrated photonic circuits<sup>19-21</sup>. Moreover, the inclusion of a layer with different optical or geometrical characteristics as a defect inside PhC structure leads to breaking its periodicity which gives rise to the localization of some frequency modes known as defect modes inside the PBG<sup>20,21</sup>. Meanwhile, the optical properties of these modes including their number, position and full width are significantly dependent on the thickness and refractive index of the defect layer.

As the defect layer is localized between symmetric structures of a 1D PhC structure, the modes decay rapidly and the EMWs are trapped in the distance between these mirrors<sup>16</sup>. Due to the combarable between this distance and the wavelength, the allowed modes are quantized. As a result, resonant states are created within the PBG. The resonant states are very sensitive to a small change of refractive index of the defect layer and its thickness as well, which makes the defect-based PhC as the suitable candidate for realizing sensing applications.

This work presents a theoretical analysis of high-sensitive magnetic field sensor utilizing the Transfer Matrix Method (TMM). Here, we have introduced a defect layer of an n doped Si inside a 1D PhC structure designed from 8-unit cells. Here, each unit cell comprises two layers of  $\text{SiO}_2$  and GaAs. The main novelty of this work lies in exploiting the enhanced Faraday effect in n-doped Si to achieve highly sensitive and tunable magnetic field sensing within a 1D PhC structure. Unlike previous magnetic field sensors based on 1D PCs, which primarily use magneto-optical materials, our design integrates precisely engineered doping levels in Si to significantly boost its magneto-optical response through free-carrier interactions. This enables a pronounced, magnetic-field-induced shift in the photonic bandgap and transmission spectrum. Further, all the geometrical parameters are meticulously optimized to achieve a maximum sensitivity. The results revealed that the optimized structure has a very good performance for example the sensitivity reaches  $2.91 \mu\text{m}/\text{Tesla}$  and detection limit decreases to  $0.0041 \text{ Tesla}$ . Moreover, to our knowledge, this is the first demonstration where n-doped Si Faraday effect is studied for high-performance magnetic field sensing in a 1D PhC framework. Additionally, the numerical findings demonstrate that the tolerance in the thicknesses of PhC constituent materials is almost unaffected on the sensitivity and may be on the overall performance of the designed sensor as well. Therefore, we believe that our designed sensor is robust against the structural disorders and the geometrical variations as well.

## Structure design and mathematical model

### Structure design

In this section, we present the structural design of the proposed sensor, which consists of 1D defective PhC. As illustrated in Fig. 1, the structure is envisaged with  $\text{SiO}_2$  as a first layer and GaAs as a 2nd layer, and the total number of periods is  $N=4$  as along the  $x$ -direction. The thickness of  $\text{SiO}_2$  and GaAs are taken as  $d_1 = 19 \mu\text{m}$  and  $d_2 = 8.5 \mu\text{m}$ , respectively, whereas the refractive index of  $\text{SiO}_2$  and GaAs are considered as  $n_1$  and  $n_2$ , respectively. The lattice constant ( $d$ ) of each unit cell is denoted as,  $d = d_1 + d_2$ . The defect layer, which is sandwiched between the two identical PhCs, is designed from an n-doped Si layer of carrier concentration ( $n_i = 1.5 \times 10^{16} \text{ m}^{-3}$ ) and doping concentration ( $N_d = 10^{23} \text{ m}^{-3}$ ). The dielectric constant of the material is  $\epsilon_\infty = 11.7$ , while the effective masses of electron and holes are  $m_e = 0.26m_0$  and  $m_h = 0.34m_0$ , respectively, where  $m_0$  represents the free electron mass,  $m_0 = 9 \times 10^{-31} \text{ Kg}$ . Additionally, the thickness of the defect layer ( $d_d$ ) is selected as  $40 \mu\text{m}$  and the damping frequencies  $\gamma_e = 7.35 \times 10^9 \text{ Hz}$ ,  $\gamma_h = 8.75 \times 10^9 \text{ Hz}$ . Wherein, the final layer in the structure is the glass substrate, which has a refractive index  $n_s = 1.52$ <sup>10</sup>. Here, the electromagnetic waves (EMWs) in range between 55 THz and 120 THz incident normally onto the structure.

### Materials selection

The selection of  $\text{SiO}_2$  and GaAs for the proposed design is driven by their complementary physical, acoustic, and electronic properties, which are critical for achieving high-performance sensing at the targeted frequencies.  $\text{SiO}_2$  offers low acoustic impedance, low density, and high transparency to surface acoustic waves, making it ideal for enhancing wave confinement and minimizing propagation losses<sup>45</sup>. Its amorphous structure also

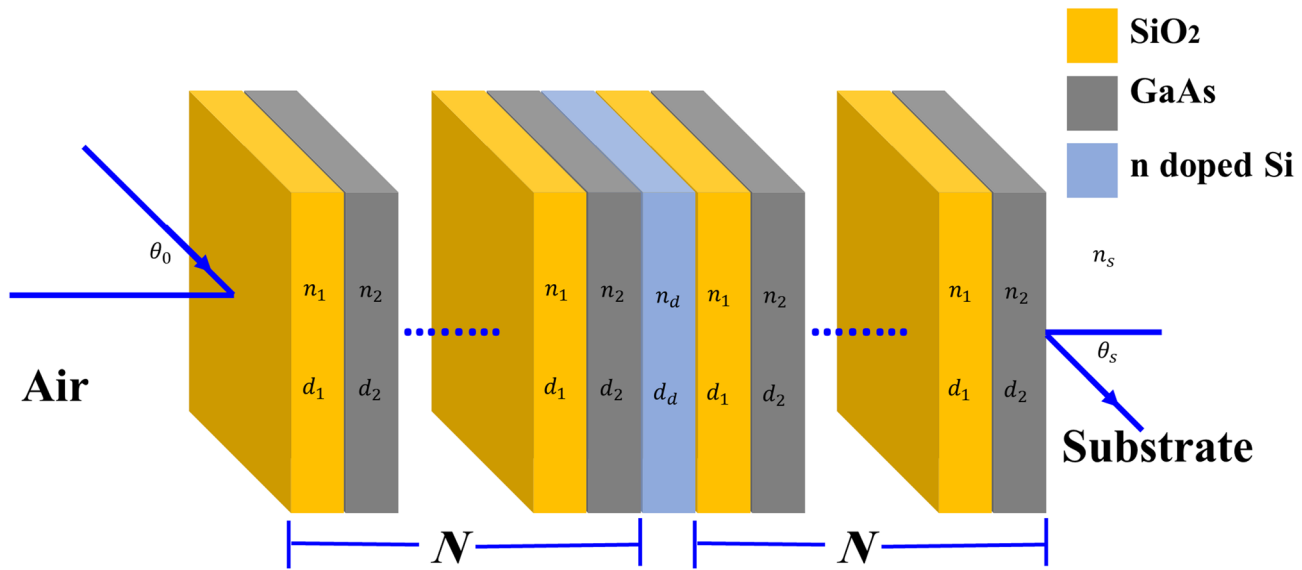


**Fig. 1.** 3D schematic description of the designed magnetic field sensor in which an n-doped Si defect layer is embedded between two identical 1D PhC structure comprising two layers of SiO<sub>2</sub> and GaAs in each unit cell.

provides mechanical stability and excellent thermal insulation, which is beneficial for maintaining consistent performance over temperature variations. On the other hand, GaAs is a piezoelectric semiconductor with high electron mobility and strong electromechanical coupling, which enables efficient detection<sup>46</sup>. Its crystalline structure supports precise photonic bandgap engineering, which allows the device to operate effectively at specific frequencies. Moreover, GaAs substrates are well-established in microfabrication, ensuring compatibility with existing semiconductor processing technologies. The combination of SiO<sub>2</sub> and GaAs enables a high acoustic impedance contrast, which is essential for strong photonic bandgap formation and improved wave scattering, which directly enhances the sensitivity.

The defect layer is designed with n-doped Si to exploit its tunable free-carrier concentration, which directly affects its refractive index and conductivity through the plasma dispersion effect. Under an applied magnetic field, the charge carriers experience the magneto-optic (Hall) effect, leading to measurable changes in optical and electrical properties. N-doped Si offers high carrier mobility, compatibility with standard microfabrication processes, and low-cost integration with other semiconductor components<sup>47</sup>. Its adjustable doping level enables precise control over sensitivity and operating range. This makes n-doped Si an ideal choice for achieving strong magnetic field responsiveness while maintaining the structural stability and fabrication feasibility in the proposed sensor.

### Mathematical model

Under the influence of an external magnetic field, the mathematical analysis of the interaction of the EMWs with the 1D defective PhCs is formulated based on the transfer matrix method (TMM) and the Faraday geometry. TMM is widely regarded as an effective approach to study the reflection and the transmission coefficients for multilayer structures<sup>10,16,23–25</sup>. Using TMM, it is easy to study the electric (TE) and magnetic (TM) amplitudes associated with both incident and transmitted EMWs at the boundaries of the whole structure<sup>17,23,26</sup>. Subsequently, we have introduced the total transfer matrix (A) according to TMM as following<sup>10,24</sup>:

$$A = (Z)^N D (Z)^N = \begin{pmatrix} A_{11} & A_{12} \\ A_{21} & A_{22} \end{pmatrix} \quad (1)$$

Where (Z)<sup>N</sup> and D represent matrices that describe the whole structure of PhCs and the defect layer, respectively. The terms  $A_{11}$ ,  $A_{12}$ ,  $A_{21}$ , and  $A_{22}$  constitute the total transfer matrix (A). Meanwhile, the transfer matrix for one period of the PhC structure is given by:

$$(Z) = \begin{pmatrix} \cos(1) & (-i/p_1)\sin(1) \\ -ip_1\sin(1) & \cos(1) \end{pmatrix} \begin{pmatrix} \cos(2) & (-i/p_2)\sin(2) \\ -ip_2\sin(2) & \cos(2) \end{pmatrix} \quad (2)$$

Hence,  $\phi_\iota$  is the wave vector ( $\phi_\iota = \frac{2\pi d_\iota n_\iota}{\lambda} \cos\theta_\iota$ ), and  $p_\iota$  is the effective optical impedance ( $p_\iota = n_\iota \cos\theta_\iota$ ), for the TE polarization<sup>10,25</sup>  $\iota = 1, 2$ .

Then, according to Chebyshev polynomials the transfer matrix for N periods of the 1D PhC structure can be expressed as<sup>24</sup>:

$$(Z) N = \begin{pmatrix} z_{11} \beta_{N-1}(\delta) - \beta_{N-2}(\delta) & z_{12} \beta_{N-1}(\delta) \\ z_{21} \beta_{N-1}(\delta) & z_{22} \beta_{N-1}(\delta) - \beta_{N-2}(\delta) \end{pmatrix} \quad (3)$$

$$= \begin{pmatrix} z_{11} & z_{12} \\ z_{21} & z_{22} \end{pmatrix}$$

$$\text{Here, } \beta_N = \frac{\sin[(N+1)\cos^{-1}(\delta)]}{\sqrt{1-\delta^2}} \text{ and } \delta = \frac{z_{11} + z_{22}}{2}.$$

Therefore, the transfer matrix of the defect layer can be written as:

$$D = \begin{pmatrix} \cos(d) & (-i/p_d)\sin(d) \\ -ip_d\sin(d) & \cos(d) \end{pmatrix} = \begin{pmatrix} d_{11} & d_{12} \\ d_{21} & d_{22} \end{pmatrix} \quad (4)$$

Hence,  $\phi_d = \frac{2\pi d_d n_d}{\lambda} \cos\theta_d$ , and  $p_d = n_d \cos\theta_d$ . The transmission coefficient ( $t$ ), which is a function in elements of the characteristic matrix, can be given as<sup>27,28</sup>:

$$t = \frac{2p_0}{(A_{11} + A_{12}p_s)p_0 + (A_{21} + A_{22}p_s)} \quad (5)$$

Where,  $p_0$  and  $p_s$  are the effective optical impedance for air and substrate layer, respectively. Finally, the transmissivity ( $T$ ) of the structure can be calculated based on the following formula<sup>29</sup>:

$$T = \frac{p_0}{p_s} |t|^2 \quad (6)$$

Additionally, according to the Faraday geometry, the relative permittivity ( $\epsilon$ ) of a n-doped semiconductor material can be calculated as<sup>10,13,19,30,31</sup>:

$$\epsilon_{\pm}(\omega) = \epsilon_{\infty} \left( 1 - \frac{\omega_{pe}^2}{\omega(\omega \mp \omega_c - \gamma_e)} - \frac{\omega_{pe}^2}{\omega(\omega \mp \omega_c - \gamma_h)} \right) \quad (7)$$

Where,  $\omega_{pe(h)}^2$  is the electrons (holes) plasma frequency<sup>32</sup> that can be written as:

$$\omega_{pe(h)}^2 = \frac{n_{e(h)}e^2}{m_{e(h)}\epsilon_0\epsilon_{\infty}} \quad (8)$$

Here,  $e$  and  $\epsilon_0$  represent the electron charge and the permittivity of the vacuum, respectively. Meanwhile, the cyclotron frequency  $\omega_c$  is determined as a function of the magnetic field intensity  $B$ , given by<sup>33</sup>:

$$\omega_c = \frac{e}{m_e} B \quad (9)$$

Subsequently, the refractive index of the n-doped semiconductor material is calculated as:

$$n_d = \sqrt{\epsilon_{\pm}(\omega)} \quad (10)$$

## Results and discussions

We employ Faraday effect in n-doped silicon to accomplish highly tunable magnetic field sensor using 1D PhC. The Faraday effect was chosen because it offers a strong, linear magneto-optical response in transmission geometry, which perfectly matches the operating principle of 1D PhC. Unlike MOKE, which is reflection-based, and the Voigt effect, which is weaker and quadratic with field strength, the Faraday effect enables efficient, high-sensitivity modulation<sup>48]-[49</sup>. In n-doped Si, the free carriers significantly enhance this effect and produce a noticeable change in the refractive index and photonic bandgap. Moreover, Faraday effect avoids reliance on exotic materials, ensuring CMOS compatibility and easy integration. These factors make the Faraday effect the most effective choice for our magnetic field sensor design. In this section, we present the optimization of the designed sensor structure and thoroughly analyzed its performance to verify the ability and the accuracy of the proposed magnetic field sensor.

## Optimization of sensor parameters

To achieve highest performance, we optimize the sensor parameters according to the performance tools. Initially, we consider the sensor structure as [ (MgF<sub>2</sub> + GaAs)<sup>N=10</sup> / n-doped Si / (MgF<sub>2</sub> + GaAs)<sup>N=10</sup> ]. Here, MgF<sub>2</sub> and GaAs layers form the unit cell of the PhC with periodicity  $N=10$ , and atomic density of the defect layer  $N_d=1 \times 10^{23} \text{ m}^{-3}$  in case of normal incidence of EMWs. All parameters of the sensor including the thicknesses of different layers,  $N_d$  and the incident angle of EMWs are optimized. The structure optimization is extensively studied in the following subsections.

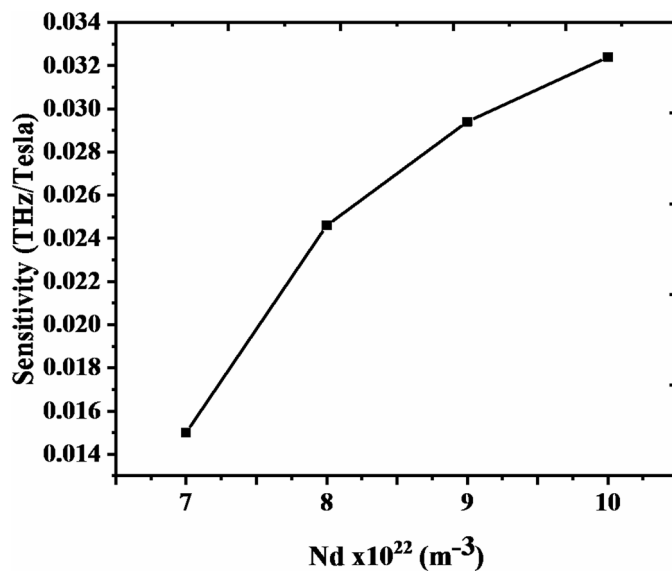


**Fig. 2.** The sensitivity response versus the impact of different values of doping concentration of the n-doped Si.

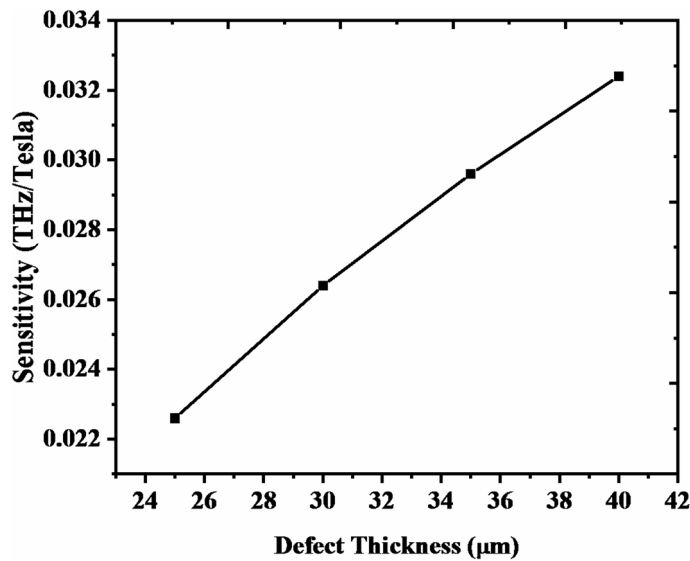


**Fig. 3.** The effect of the defect layer thickness on the sensor's sensitivity.

#### *Optimization of the doping concentration and thickness of the defect layer*

Here, we start the optimization process by checking the effect of doping concentration of the n-doped Si on the sensor sensitivity as shown in Fig. 2. Specifically, we took the values of  $N_d = [7, 8, 9, 10] \times 10^{22} \text{ m}^{-3}$  and observed the variation in the sensitivity. As seen in Fig. 2, the sensitivity increases gradually with increase in the atomic density, and the maximum sensitivity reaches up to 0.0324 THz/Tesla at  $N_d = 10^{23} \text{ m}^{-3}$ . Therefore,  $N_d = 10^{23} \text{ m}^{-3}$  is selected as the optimal value for our magnetic field sensor.

Then, we survey the impact of defect layer thickness ( $da$ ) on the sensitivity of the structure. According to Fig. 3, the sensitivity is affected by changing the thickness of the defect layer. In particular, when  $da = 25 \mu\text{m}$ , the sensitivity = 0.0226 THz/Tesla and by increasing ( $da$ ) the sensitivity keeps increasing until the optimal thickness of 40  $\mu\text{m}$  is reached. This confirms that the highest sensitivity (0.0324 THz/Tesla) occurred at  $N_d = 10^{23} \text{ m}^{-3}$  and defect layer thickness  $da = 40 \mu\text{m}$ .

#### *Optimization of the types of material of phc unit cell*

Furthermore, we optimize the unit cell of PhC by checking the types of the dielectric layers, periodicity and its thickness for each one according to the highest sensitivity.

Dielectric material	Refractive index
$\text{MgF}_2$	2.05
$\text{SiO}_2$	2.105
$\text{Al}_2\text{O}_3$	3.39
$\text{SrF}_2$	2.49
GaAs	3.58
$\text{GdF}_3$	3.08

**Table 1.** The refractive indices of the different dielectric materials through the operating wavelengths of the designed sensor<sup>35,50–56</sup>.

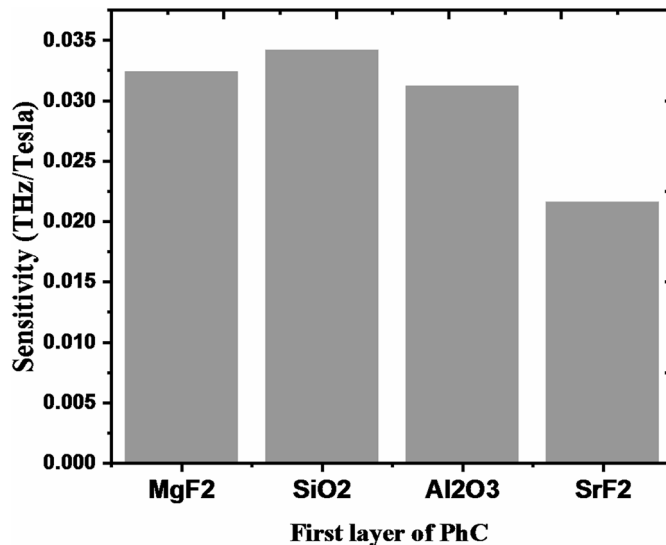


**Fig. 4.** The role of the refractive index of the 1st layer in each unit cell of PhC structure on the sensitivity of the designed sensor.

**The First layer of the unit cell** Firstly, we fix the second layer as GaAs, and then change the dielectric type of the first layer. Notably, we select different dielectric materials like  $\text{MgF}_2$ ,  $\text{SiO}_2$ ,  $\text{Al}_2\text{O}_3$ , and  $\text{SrF}_2$  based on their refractive index contrast, because the high contrast between the constituent dielectric materials must be sufficiently large to enhance the Bragg reflection and form a wide PhC band gap<sup>34</sup>.

In this regard, we have optimized different dielectric materials to be embedded as the first layer of the designed PhC structure. Here, the mainstay towards the dependence on a specified material is mainly based on the recorded sensitivity. Meanwhile, Table 1 summarizes the indices of refraction for the selected materials within the frequencies of interest<sup>35,50–56</sup>. Here, the selected materials provide a stable response for their indices of refraction over the operating wavelengths of the designed sensor as listed in Table 1. This response could be of a potential interest through the experimental verification of the designed sensor. Then, Fig. 4 displays the different values of the sensitivity based on the inclusion of some different dielectric materials as a first layer inside each unit cell of the designed PhC structure. In contrast, the second layer in each unit cell of the designed PhC structure is kept as GaAs. In this regard, the inclusion  $\text{SiO}_2$  as the first layer of PhC design gives rise to some significant improvements on the sensitivity of the designed sensor compared to other materials such as  $\text{MgF}_2$ ,  $\text{Al}_2\text{O}_3$  and  $\text{SrF}_2$ . Here, the sensitivity of the designed structure increases to 0.0342 THz/Tesla compared to the results investigated in Figs. 2 and 3. Therefore,  $\text{SiO}_2$  presents the optimum choice as the first layer in each unit cell of the designed PhC towards the largest sensitivity.

**The second layer of the unit cell** Following a similar optimization procedure, we analyzed the second layer of the photonic crystal (PhC) unit cell. The first layer was fixed as  $\text{SiO}_2$ , having previously been identified as the optimal configuration. To determine the most suitable material for the second layer, we evaluated the sensor's sensitivity using various dielectric materials including GaAs,  $\text{GdF}_3$ , and  $\text{SrF}_2$  whose refractive indices are listed in Table 1. The results, as illustrated in Fig. 5, indicate that GaAs yields the highest sensitivity, while  $\text{SrF}_2$  demonstrates the lowest. Consequently, GaAs was selected as the optimal material for the second layer in the PhC design. Thus, the unit cell of the PhC is designed using  $\text{SiO}_2$  and GaAs due to their high effectiveness in enhancing the sensor's sensitivity.

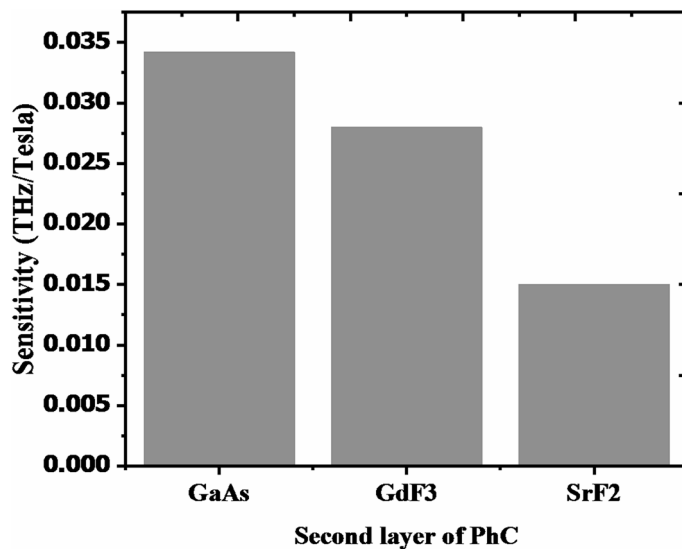


**Fig. 5.** The role of the refractive index of the 2nd layer in each unit cell of PhC structure on the sensitivity of the designed sensor.

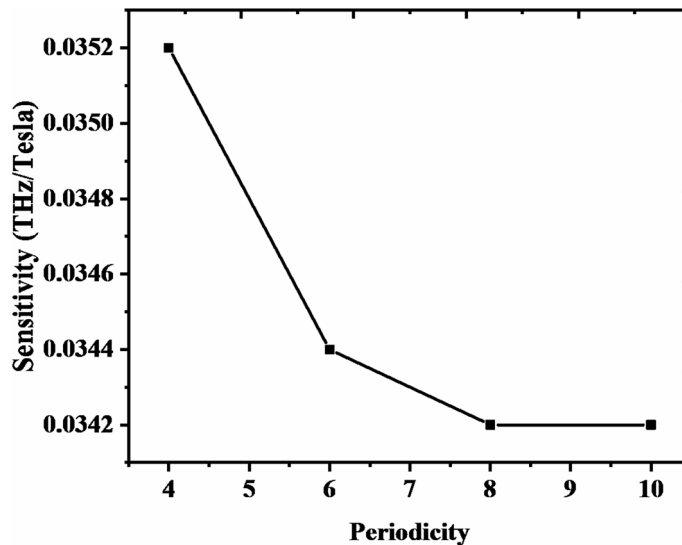


**Fig. 6.** The impact of using different numbers of periods on the sensitivity of the sensor.

#### *Optimization of the periodic number of the phc unit cell*

Moreover, we study the effect of the number of periods of the unit cell ( $\text{SiO}_2/\text{GaAs}$ ) on the sensor sensitivity. It can be seen from the Fig. 6 that the sensitivity increases from 0.0342 THz/Tesla to 0.0352 THz/Tesla by decreasing the number of periods from 10 to 4. As a result, the sensor performance is enhanced at 4 periods of the unit cell, therefore we selected this optimal value to design our structure.

#### *Optimization of the layers' thickness of the phc unit cell*

Following the optimization of unit cell materials and its periodicity, we optimize the layers' thickness which plays a critical role as a lattice constant of the structure's unit cell.

**The thickness of  $\text{SiO}_2$**  Initially, we optimize the thickness of the first layer ( $\text{SiO}_2$ ) by checking the impact of different thicknesses like 16  $\mu\text{m}$ , 18  $\mu\text{m}$ , 19  $\mu\text{m}$ , and 20  $\mu\text{m}$  on the sensitivity, while keeping the other geometrical parameters as constant. As illustrated in Fig. 7, the sensitivity at 16  $\mu\text{m}$  is 0.0352 THz/Tesla. Then, it increases with thickness and reaches a maximum of 0.0368 THz/Tesla at 19  $\mu\text{m}$ . Beyond this thickness, the sensitivity begins to decrease. Therefore, 19  $\mu\text{m}$  is identified as the most effective thickness based on the sensor sensitivity results.

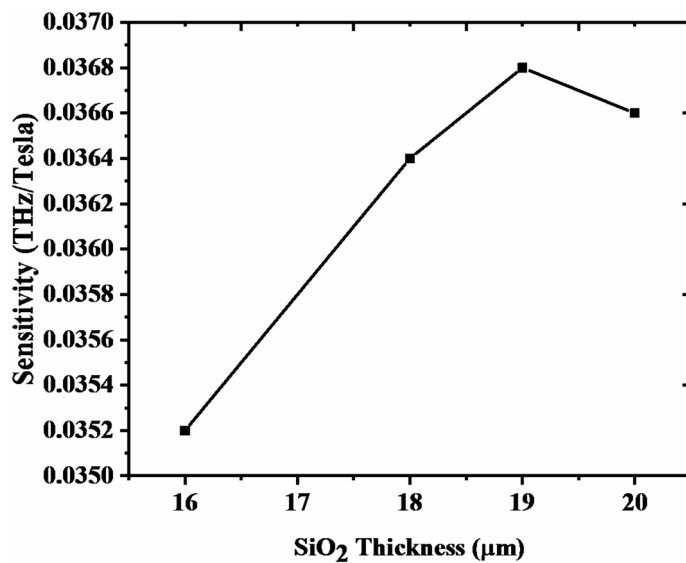


**Fig. 7.** The effect of different thicknesses of the SiO<sub>2</sub> layers on the sensor sensitivity.

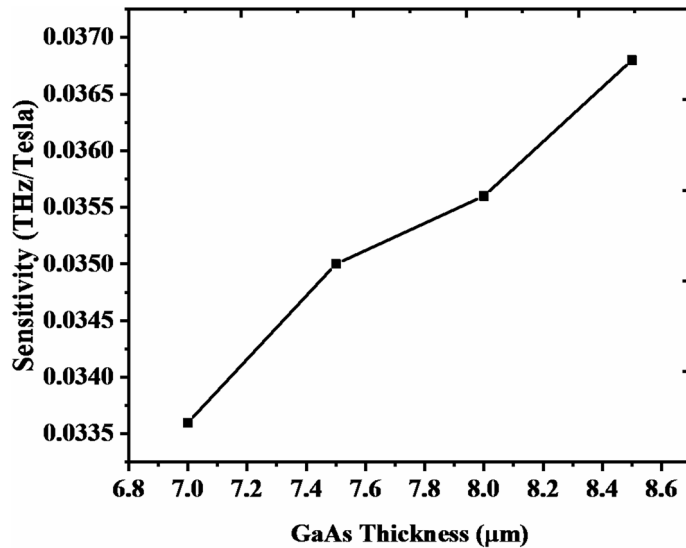


**Fig. 8.** The effect of different thicknesses of the GaAs layer on the sensor sensitivity.

**The thickness of GaAs** The thickness of the second layer (GaAs) is optimized by following the same procedure as the thickness of the first layer. Specifically, we observed the effect of thicknesses like 7, 7.5, 8, and 8.5 μm on the sensor's sensitivity and it is found that the sensitivity gradually increases with the thickness as illustrated in Fig. 8. This led to select 8.5 μm as the optimal thickness for the second layer ( $d_2$ ). Finally, the optimal thickness of the structure unit cell is found to be  $a = 19 \mu\text{m} + 8.5 \mu\text{m} = 27.5 \mu\text{m}$ . This thickness significantly enhances the sensor's sensitivity, raising it to a high value of 0.0368 THz/Tesla.

#### *Optimization of the incident angle of the interacting electromagnetic waves*

Finally, we optimize the angle of the incidence. That is an important factor, which greatly affects sensor performance. We measured the sensitivity at different angles such as 0°, 20°, 40°, and 60°, which is demonstrated in Fig. 9. We observed that the sensitivity decreases to 0.034 THz/Tesla by increasing the incident angle from 0° to 60°. So, it is confirmed that a maximum sensitivity of 0.0368 THz/Tesla is attained in case of the normal incident of the interacting EMWs.

From the above results, we concluded that optimal value of sensitivity is accomplished by designing the structure with SiO<sub>2</sub> and GaAs as the dielectric layers, each with a thickness 19 μm and 8.5 μm, respectively. Moreover, the optimum thickness of the defect layer and its atomic density are found to be 40 μm and 10<sup>23</sup> respectively. The number of the periodicity of the structure unit cell is 4, and the optimized incident angle is 0°. This optimization achieves a maximum sensitivity of 0.0368 THz/Tesla.

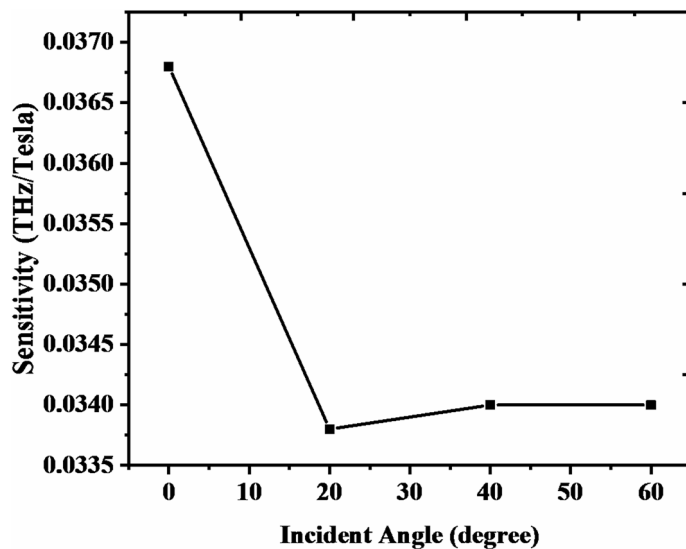


**Fig. 9.** The role of the angle of incident on the sensitivity of the designed structure.

### Numerical analysis and the discussion

Depending on the optimization of the geometrical parameters, the overall performance of the sensor is presented in this section in detail. Consequently, the performance parameters which we measured include sensitivity (S), quality factor (Q), signal-to-noise ratio (SNR), detection limit (DL), sensor resolution (SR), and figure of merit (FOM) to evaluate the performance of the sensor<sup>30,36–39</sup>. Meanwhile, the sensitivity, quality factor, and figure of merit are considered key parameters, as their calculations depend on the resonance position, which shifts with varying magnetic field strength<sup>40,41</sup>.

To begin with, the sensitivity (S) determines the difference of the resonant wavelength according to change the strength of the magnetic field, and can be expressed as:

$$S = \frac{\Delta \lambda_{res}}{\Delta B} \quad (11)$$

Where,  $\Delta\lambda_{res}$  is the change in the resonant wavelength, and  $\Delta B$  is the change of the magnetic field strength. Furthermore, quality factor (Q) is defined as the ratio of  $\lambda_{res}$  to the full width at half maximum (FWHM) of the defect mode resonant wavelength. Based on this, Q is given by:

$$Q = \frac{\lambda_{res}}{FWHM} \quad (12)$$

Another, important parameter of the sensor is the figure of merit (FOM), and it is calculated as following:

$$FOM = \frac{S}{\Delta FWHM} \quad (13)$$

Moreover, the signal-to-noise ratio (SNR) is another performance parameter, which we are interested to measure. SNR is calculated as the ratio between the resonance signal and the background noise. We can calculate it using the following formula:

$$SNR = \frac{\Delta \lambda_{res}}{\Delta FWHM} \quad (14)$$

In addition to that, the detection limit (DL) is a significant parameter, which indicates the ability of the sensor to detect the smallest variation in the magnetic field, expressed as:

$$DL = \left( \frac{2}{S} \right) \left( \frac{FWHM}{3(SNR)^{0.25}} \right) \quad (15)$$

Furthermore, the sensor resolution (SR) is defined as following:

$$SR = (DL)(S) \quad (16)$$

Owing to the presence of a defect layer in the proposed 1D PhC structure, a resonant state is appeared with in the bandgap (defect modes), which can be seen in Fig. 10. These modes help in measuring the sensor

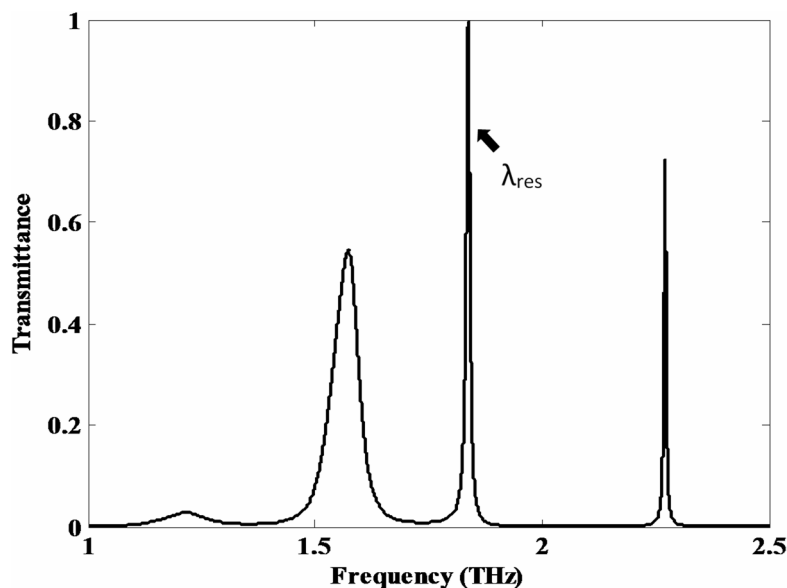


**Fig. 10.** The light transmission spectrum of the 1D PhC magnetic field sensor versus the frequency of the propagating EMWs at the optimum values of the governing parameters.

performance due to the shift of the resonant state that caused by changing the strength of the magnetic field. Then, we have considered in Fig. 11 the magnetic field distribution through the designed PhC structure. In Fig. 11, a comprehensive analysis of the magnetic field distribution within our optimized structure is conducted, comprising 1D PhCs integrated with a defect layer fashioned from n-doped silicon. Figure 11a elucidates the precise localization of the magnetic field within the defect layer derived from n-doped silicon, under the compelling influence of an incident frequency of  $1.09 \times 10^{12} \text{ THz}$ . Subsequently, in Fig. 11b, the incident frequency is heightened to  $1.27 \times 10^{12} \text{ THz}$ , thereby effecting a notable transference of the magnetic field localization from the defect layer towards the layer of lower refractive index, specifically  $SiO_2$ . The progression of this phenomenon is meticulously charted. Lastly, Fig. 11c demonstrates a further escalation in the incident frequency to  $2.28 \times 10^{12} \text{ THz}$ , instigating a consequential shift in the magnetic field localization from the lower refractive index layer ( $SiO_2$ ) to the layer of higher refractive index, denoted as GaAs. This distinctive relocation of the magnetic field is brightly represented in the reduced graphical representation.

In greater depth, the optical characteristics of the transmission spectrum are depicted in Fig. 12. The transmission spectrum is clearly affected as the external applied magnetic field which increases from 0 Tesla to 10 Tesla. As can be observed from the figure, the position of the defect mode is shifted towards the higher frequencies, and the intensity decreases by increasing the strength of the magnetic field above 5 Tesla (T). The nature of shift of defect mode frequency can be described using standing wave condition<sup>41</sup>,

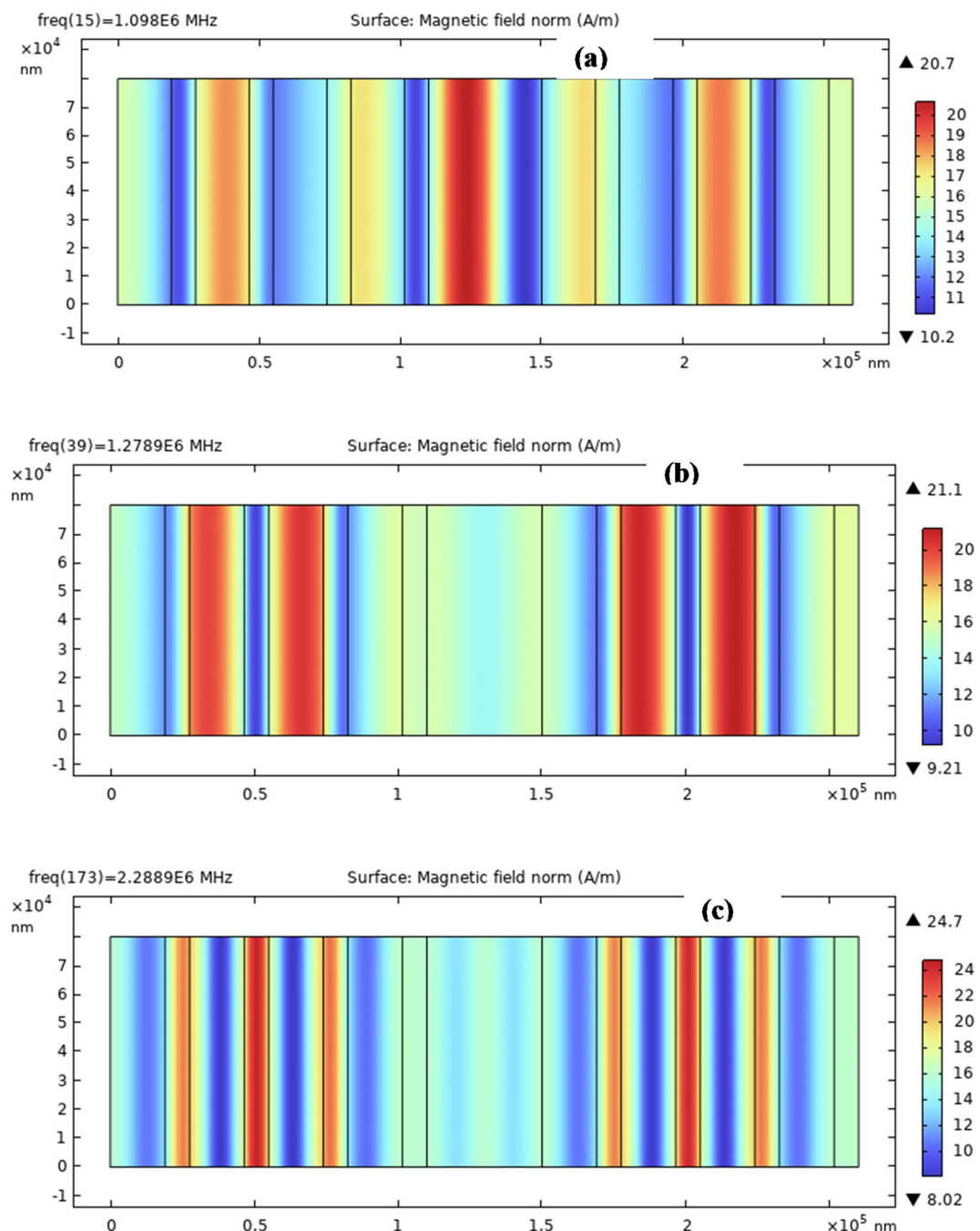
$$\gamma = p\lambda_{res} = n_{eff}\tau \quad (17)$$

Where,  $\gamma$  and  $\tau$  denote the optical and geometrical path difference respectively. The notion  $p$  indicates an integer,  $\lambda_{res}$  represents the resonance wavelength, and  $n_{eff}$  stands for the effective refractive index. The value of  $n_{eff}$  increases when the defect layer is exposed to the high intensity of magnetic field, which results in shift in  $\lambda_{res}$  towards higher value to keep  $\gamma$  fixed.

Here, the resonant wavelength for 3 T, 5 T, 7 T, and 10 T is 155.5  $\mu\text{m}$ , 149.6  $\mu\text{m}$ , 143.4  $\mu\text{m}$ , and 134.2  $\mu\text{m}$ , respectively. By applying these values in Eq. 11 to Eq. 16, we measured the performance parameters like S, FWHM, Q, FOM, SNR, DL, and SR, which are listed in Table 2. It was observed that the sensor's sensitivity increases with the strength of the applied magnetic field, reaching a maximum value of 2.91  $\mu\text{m}/\text{Tesla}$ , which underscores its strong responsiveness to magnetic field variations. Furthermore, high quality factor (Q-factor) values of 1633 were recorded at magnetic field strengths of 7 T and 10 T, indicating narrow resonance linewidths and enhanced signal selectivity. The figure of merit (FOM) also exhibited significant improvement, validating the effectiveness of the optimized structural design. Additionally, a high signal-to-noise ratio (SNR) of 291 was achieved at 10 T, demonstrating the sensor's capability to reliably differentiate signal from background noise. With a detection limit (DL) of 0.0055 Tesla and a spectral resolution (SR) of 0.016  $\mu\text{m}$ , the sensor exhibits exceptional precision and can identify minute variations in the magnetic field, thereby confirming its high-performance potential.

### Fabrication tolerance

Now, we turn our attention to discussing the role of thickness tolerance on the sensitivity of the designed sensor. Notably, fabrication tolerance could have a distinct effect on both optical response of the designed structure and detection accuracy as well in many diverse applications. Actually, the tolerance in the thickness of a distinct

**Fig. 10.** (continued)**Fig. 11.** The magnetic field distribution for the optimum structure at different incident frequencies, (a) the frequency  $= 1.09 \times 10^{12} \text{ THz}$ , (b) the frequency  $= 1.27 \times 10^{12} \text{ THz}$ , and (c): the frequency  $= 2.28 \times 10^{12} \text{ THz}$ .

layer is described as the range of an acceptable change in the thickness of this layer. Meanwhile, we have considered the role of thickness tolerance on the different layers of our designed magnetic field sensor. Here, Table 3 demonstrates the changes in the sensitivity of the designed sensor due to the tolerance in the thickness of GaAs. In this regard, the changes in the thickness of GaAs layers vary from  $-100 \text{ nm}$  to  $+100 \text{ nm}$ . The results investigated in Table 3 show that the tolerance in the thickness of GaAs layers provides a little effect on the sensitivity of the designed sensor. This effect appears in a small variation of  $0.0004 \text{ THz/Tesla}$  at maximum

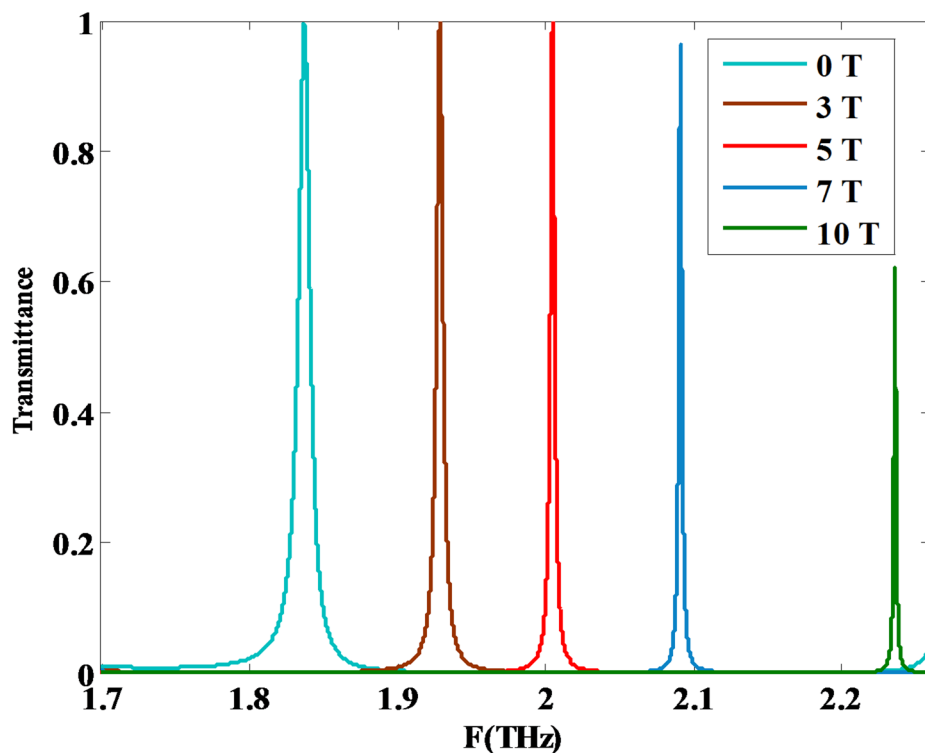


**Fig. 12.** The light transmission spectrum of the defective 1D PhC sensor as a function of the frequency at different magnetic field intensities.

Parameter	3 Tesla	5 Tesla	7 Tesla	10 Tesla
Sensitivity ( $\mu\text{m}/\text{Tesla}$ )	2.6	2.74	2.84	2.91
FWHM ( $\mu\text{m}$ )	0.5	0.3	0.1	0.1
Q	326.6	544.33	1633	1633
SNR	15.6	45.66	199	291
DL (Tesla)	0.065	0.028	0.0062	0.0055
SR ( $\mu\text{m}$ )	0.169	0.077	0.018	0.016
FOM (Tesla) $^{-1}$	5.2	9.26	28.4	29.1

**Table 2.** The performance of the 1D D-PhC sensor at different values of the applied magnetic field.

Fabrication tolerance (nm)	Sensitivity (THz/Tesla)
- 100	0.0364
- 80	0.0366
- 60	0.0364
- 40	0.0366
- 20	0.0366
Optimized thickness (8.5 $\mu\text{m}$ )	0.0368
+ 20	0.0366
+ 40	0.0366
+ 60	0.0366
+ 80	0.0368
+ 100	0.0366

**Table 3.** The role of fabrication tolerance of GaAs layers thickness on the sensitivity of the designed sensor.

Fabrication tolerance (nm)	Sensitivity (THz/Tesla)
- 100	0.0364
- 80	0.0366
- 60	0.0366
- 40	0.0366
- 20	0.0366
Optimized thickness (19 $\mu\text{m}$ )	0.0368
+ 20	0.0366
+ 40	0.0366
+ 60	0.0366
+ 80	0.0366
+ 100	0.0364

**Table 4.** The role of fabrication tolerance of  $\text{SiO}_2$  layers thickness on the sensitivity of the designed sensor.

Fabrication tolerance (nm)	Sensitivity (THz/Tesla)
- 100	0.0364
- 80	0.0364
- 60	0.0364
- 40	0.0364
- 20	0.0366
Optimized thickness (40 $\mu\text{m}$ )	0.0368
+ 20	0.0366
+ 40	0.0366
+ 60	0.0366
+ 80	0.0366
+ 100	0.0366

**Table 5.** The role of fabrication tolerance of n doped Si layers thickness on the sensitivity of the designed sensor.

Ref	Structure	Sensing principle	Sensitivity ( $\mu\text{m}/\text{T}$ )	Year
<a href="#">6</a>	Photonic crystal fiber	Plasmonics effect	0.02175	2022
<a href="#">42</a>	Tapper fiber optic tweezer	Wavelength shift	0.258	2025
<a href="#">43</a>	Metal-Insulator-Metal (MIM) waveguide	Plasmonics effect	0.4911	2024
<a href="#">18</a>	1D PhC	Taam/Fano resonance	0.057	2025
<a href="#">44</a>	Febry-Perot interferometer	Spectral and intensity shift	$1.1 \times 10^{-6}$	2024
Our sensor	Defect-based 1D PhC	Bandgap shift	2.91	This work

**Table 6.** A brief comparison with the available published papers in the vicinity of the investigated sensitivity.

through the sensitivity of the designed magnetic field sensor. In contrast, Table 4 investigates the same effect for  $\text{SiO}_2$  layers. The behavior of sensitivity for tolerance of  $\text{SiO}_2$  is like that of GaAs layers. Finally, Table 5 investigates the same role for n doped Si layers. The results obtained for n doped Si are like those investigated for GaAs and  $\text{SiO}_2$ . To sum up, the tolerance in the thicknesses of PhC constituent materials is almost unaffected on the sensitivity and may be on the overall performance of the designed sensor as well. Therefore, we believe that our designed sensor is robust against the structural disorders and the geometrical variations as well. Moreover, we believe that tolerance of 100 nm during the manufacturing process is a very large value. In particular, some fabrication techniques such as the atomic layer deposition (ALD) could be promising for sufficient control of very small thicknesses which in turn may be of a significant contribution towards achieving precise tailoring of interfaces with great accuracy for fabricating thin films with tight tolerances<sup>[57,58](#)</sup>.

### Comparative analysis

We compare the sensor's performance with recently published different photonic structures for magnetic field sensing applications, which is given in Table 6. From this table, it is confirmed that the magnetic field sensitivity of the proposed sensor exceeds that of most previous works by approximately two orders of magnitude. In addition to the high sensitivity, the use of n-doped Si in our design enhances the Q-factor up to 1633 at 7 T and

10 T due to the lower optical absorption of doped semiconductors in the THz region. The high sensitivity of  $2.91 \mu\text{m}/\text{T}$  arises mainly due to the combined effects of the enhanced Faraday response in heavily n-doped Si and the strong field coupling provided by the optimized 1D PhC. The high doping level significantly increases the magneto-optical coefficient, producing a larger refractive index change under a given magnetic field. This, in turn, results in a more pronounced photonic bandgap shift compared to conventional designs. Additionally, careful optimization of layer thicknesses and other geometrical parameters maximizes the sensitivity. The proposed sensor design has demonstrated high performance efficiency, while also offering a cost-effective and structurally simple configuration. This added simplicity in fabrication and integration enhances its appeal for practical applications in magnetic field sensing systems.

## Conclusion

In summary, the proposed magnetic field sensor designed based on the Faraday effect influencing the permittivity of n-doped silicon, which functions as a defect layer in a 1D PhC operating in the far-infrared range has been comprehensively investigated. Numerical analysis, conducted using the transfer matrix method within the Faraday geometry, was employed to examine the shift in the defect mode frequency under varying magnetic field intensities. To maximize performance, the sensor's structural parameters and the incident angle of the interacting electromagnetic waves were systematically optimized by evaluating sensitivity. Parameters such as layer thicknesses, number of periods, doping concentration, and incident angle were fine-tuned. Based on the optimization results, the final sensor configuration is defined as  $[(\text{SiO}_2 + \text{GaAs})^{N=4}/\text{n-doped Si} / (\text{SiO}_2 + \text{GaAs})^{N=4}]$ , with  $N_d = 1 \times 10^{23} \text{ m}^{-3}$ ,  $d_a = 40 \mu\text{m}$ ,  $d_1 = 19 \mu\text{m}$ ,  $d_2 = 8.5 \mu\text{m}$ , at normal incidence. The optimized sensor exhibits excellent performance metrics, achieving a sensitivity of  $2.91 \mu\text{m}/\text{Tesla}$ , a quality factor (Q) of 1633, a signal-to-noise ratio (SNR) of 291, a detection limit (DL) of 0.0055 Tesla, a spectral resolution (SR) of  $0.016 \mu\text{m}$ , and a figure of merit (FOM) of  $29.1 \text{ Tesla}^{-1}$  highlighting its strong potential for high-precision magnetic field sensing applications. Additionally, the designed sensor is robust against the structural disorders and the geometrical variations as well. In particular, the decrements in the sensitivity of the designed sensor are not exceeding over  $0.0004 \text{ THz}/\text{Tesla}$  for tolerance of 100 nm in the thickness of the considered materials.

## Data availability

The datasets used and/or analyzed during the current study available from the corresponding author on reasonable request.

Received: 12 July 2025; Accepted: 4 September 2025

Published online: 07 October 2025

## References

1. Amiri, T. Design and simulation of magnetic field sensor based on dual-core photonic crystal fiber filled ferrofluid at different ambient temperatures. *Phys. Scripta*. **100**, 025521 (2025).
2. Liu, Y. et al. High-sensitivity optical fiber magnetic field sensor based on multimode optical fiber multi Fabry-Perot interference cavities. *Opt. Express*. **31** (2), 1025–1033 (2023).
3. Yao, S. et al. Research on optimization of magnetic field sensing characteristics of PCF sensor based on SPR. *Opt. Express*. **30** (10), 16405–16418 (2022).
4. Khan, M. A. et al. Magnetic sensors-A review and recent technologies. *Eng. Res. Express*. **3** (2), 022005 (2021).
5. Popovic, R., Flanagan, J. & Besse, P. The future of magnetic sensors. *Sens. Actuators A: Phys.* **56** (1–2), 39–55 (1996).
6. Wang, D. et al. Design of photonic crystal fiber to excite surface plasmon resonance for highly sensitive magnetic field sensing. *Opt. Express*. **30** (16), 29271–29286 (2022).
7. Vatsa, R. et al. Tunable 1D ferrite photonic crystals: magnetic field control of band gaps and electromagnetic dispersion characteristics. *Phys. Lett. A*. **533**, 130219 (2025).
8. Lan, T., Ding, B. & Liu, B. Magneto-optic effect of two-dimensional materials and related applications. *Nano Select*. **1** (3), 298–310 (2020).
9. Kos, J. et al. Unveiling the transformative power of near-infrared spectroscopy in biomedical and pharmaceutical analysis: trends, advancements, and applications. *Eur. J. Pharm. Sci.* **212**, 107175 (2025).
10. Aly, H., ElSayed, H. A. & A. and Tunability of defective one-dimensional photonic crystals based on Faraday effect. *J. Mod. Opt.* **64** (8), 871–877 (2017).
11. Bondarenko, E. et al. Enhancing current sensor sensitivity using faraday effect with multiple reflections in magneto-optical crystals, EPJ Web of Conferences 318, 05007 (2025).
12. Dadoenkova, Y. S. et al. Faraday effect in bi-periodic photonic-magnonic crystals. *IEEE Trans. Magn.* **53** (11), 1–5 (2017).
13. Chang, J. P. et al. Scalable Optical Frequency Rulers with the Faraday Effect. *Photonics*, vol. 11, p. 127, (2024).
14. Hagemeyer, J. N. *Photonic Crystal Microcavities for Quantum Information Science* (University of California, Santa Barbara, 2013).
15. Taya, S. A. & Daher, M. G. Properties of defect modes of one-dimensional quaternary defective photonic crystal nanostructure. *Int. J. Smart Grid-ijSmartGrid*. **6** (2), 30–39 (2022).
16. Francis Segovia-Chaves, Juan Carlos Trujillo and Trabelsi, Y. Enhanced the sensitivity of one-dimensional photonic crystals infiltrated with cancer cells, *Materials Research Express*, vol. 10, p. 026202, (2023).
17. Saini, S. K. & Awasthi, S. K. Sensing and detection capabilities of one-dimensional defective photonic crystal suitable for malaria infection diagnosis from preliminary to advanced stage: theoretical study. *Crystals* **13** (1), 128 (2023).
18. Elsayed, H. A. et al. A promising high-sensitive 1D photonic crystal magnetic field sensor based on the coupling of Fano\Tamm resonance in far IR region. *Scientific Reports*, 15(1): p. 1977. (2025)
19. Aly, A. H., Elsayed, H. A. & El-Naggar, S. A. Tuning the flow of light in two-dimensional metallic photonic crystals based on Faraday effect. *J. Mod. Opt.* **64** (1), 74–80 (2017).
20. Xin, Y. et al. Comprehensive analysis of band gap of phononic crystal structure and objective optimization based on genetic algorithm. *Phys. B*. **667**, 415157 (2023).
21. Parvini, T. S. & Khazaei Nezhad, M. Magnetooptical properties of one-dimensional aperiodic magneto-photonic crystals based on Kolakoski sequences. *Appl. Phys. B*. **128**, 194 (2022).
22. Senouci, K. et al. Electro-optic properties of one-dimensional (1D) nonlinear perfect photonic crystals based on Lithium tantalate layer, *Optik*, vol. 265, p. 169537, (2022).

23. Aly, A. H. et al. Study on a one-dimensional defective photonic crystal suitable for organic compound sensing applications. *RSC Adv.* **11** (52), 32973–32980 (2021).
24. Born, M. & Wolf, E. *Principles of Optics: Electromagnetic Theory of Propagation, Interference and Diffraction of Light* (Elsevier, 2013).
25. Panda, A. & Segovia-Chaves, F. Defect mode modulation to detect various bacteria in defective one dimensional photonic crystals. *Rom. J. Phys.* **67**, 9–10 (2022).
26. Ramanujam, N. et al. Design of one dimensional defect based photonic crystal by composited superconducting material for bio sensing applications. *Phys. B: Condens. Matter.* **572**, 42–55 (2019).
27. Li, N. et al. Highly sensitive sensors of fluid detection based on magneto-optical Tamm state. *Sens. Actuators B.* **265**, 644–651 (2018).
28. Abadla, M. M., Abohassan, K. M. & Ashour, H. S. One-dimensional binary photonic crystals of graphene sheets embedded in dielectrics. *Phys. B: Condens. Matter.* **601**, 412436 (2021).
29. Kumar, N. & Suthar, B. *Advances in Photonic Crystals and Devices* (CRC, 2019).
30. Ramanujam, N. R. et al. Numerical characterization of 1D photonic crystal waveguide for female reproductive hormones sensing applications. *Phys. B: Condens. Matter.* **639**, 414011 (2022).
31. Pidgeon, C. *Handbook on Semiconductors*, ed. M. Balkanski. North-Holland, Amsterdam. (1980).
32. Elsayed, H. A. Quasiperiodic photonic crystals for filtering purpose by means of the n doped semiconductor material. *Phys. Scr.* **95** (6), 065504 (2020).
33. Abinash et al. Realization of sucrose sensor using 1D photonic crystal structure vis-à-vis band gap analysis. *Microsyst. Technol.* **27** (3), 833–842 (2021).
34. Joannopoulos, J. D. et al. *Molding the Flow of Light*12 (Princeton Univ. Press. Princeton, NJ [ua], 2008).
35. RefractiveIndex.Info Refractive index database. (2025).
36. Mehaney, A., Abadla, M. M. & Elsayed, H. A. 1D porous silicon photonic crystals comprising tamm/fano resonance as high performing optical sensors. *J. Mol. Liq.* **322**, 114978 (2021).
37. Ahmed, A. M. & Mehaney, A. Ultra-high sensitive 1D porous silicon photonic crystal sensor based on the coupling of tamm/fano resonances in the mid-infrared region. *Sci. Rep.* **9** (1), 6973 (2019).
38. Mehdi Keshavarz, M. & Alighanbari, A. Self-referenced Terahertz refractive index sensor based on a cavity resonance and Tamm plasmonic modes. *Appl. Opt.* **59** (14), 4517–4526 (2020).
39. White, I. M. & Fan, X. On the performance quantification of resonant refractive index sensors. *Opt. Express.* **16** (2), 1020–1028 (2008).
40. Abood, I. et al. Topological photonic crystal sensors: fundamental principles, recent advances, and emerging applications. *Sensors* **25** (5), 1455 (2025).
41. Mohamed, Z. E. A. et al. Sensing performance of Fano resonance induced by the coupling of two 1D topological photonic crystals. *Opt. Quant. Electron.* **55** (11), 943 (2023).
42. Jiang, C. et al. Optical manipulation of magnetic microspheres enables high-sensitivity fiber-optic magnetic field sensors. *Measurement* **242**, 116135 (2025).
43. Haque, M. A. et al. Numerical analysis of a metal-insulator-metal waveguide-integrated magnetic field sensor operating at sub-wavelength scales. *Sens. Bio-Sensing Res.* **43**, 100618 (2024).
44. Su, C. et al. A highly sensitive sensor based on combination of magnetostrictive material and Vernier effect for magnetic field measurement. *J. Lightwave Technol.* **42** (1), 485–492 (2024).
45. Thien, N. D. et al. Optical properties of  $\text{SiO}_2$  opal crystals decorated with silver nanoparticles. *Opt. Materials: X* **24**, 100362 (2024).
46. Isik, M. & Gasanly, N. M. Comprehensive ellipsometric analysis of linear and nonlinear optical properties of GaAs for optoelectronic and communication applications. *J. Mater. Sci.* **60**, 11435–11445 (2025).
47. Joy, J. D. et al. The potential of heavily doped n-type silicon in plasmonic sensors. *Measurement* **242**, 116049 (2025).
48. Dharmawan et al. Comparison of Magneto-Optical Faraday effect method and magnetic camera for imaging the 2-D static leakage magnetic flux density. *E-J. Nondestructive Test.*, **27**(9). (2022).
49. Alexey, K. et al. The 2022 magneto-optics roadmap. *J. Phys. D.* **55**, 463003 (2022).
50. Mashkovich, E. A., Shugurov, A. I., Ozawa, S., Estacio, E. & Tani, M. Bakunov M. I. Noncollinear electro-optic sampling of Terahertz waves in a Thick GaAs crystal. *IEEE Trans. Terahertz Sci. Technol.* **5** (5), 732–736 (2015).
51. Yahya, A. H., Balal, N., Klein, A., Gerasimov, J. & Friedman, A. Improvement of the electro-optical process in GaAs for Terahertz single pulse detection by using a fiber-coupling system. *Appl. Sci.* **11** (15), 6859 (2021).
52. Naftaly, M. & Gregory, A. Terahertz and microwave optical properties of single-crystal quartz and vitreous silica and the behavior of the Boson peak. *Appl. Sci.* **11** (15), 6733 (2021).
53. Kim, Y., Yi, M., Kim, B. G. & Ahn, J. Investigation of THz birefringence measurement and calculation in  $\text{Al}_2\text{O}_3$  and  $\text{LiNbO}_3$ . *Appl. Opt.* **50** (18), 2906–2910 (2011).
54. Yu, F. et al. The birefringence property of magnesium fluoride crystal in THz frequency region. InInfrared, Millimeter Wave, and Terahertz 7854: pp. 404–412. (2010).
55. Franta, D. et al. Škoda D. Optical characterization of gadolinium fluoride films using universal dispersion model. *Coatings* **13** (2), 218 (2023).
56. Bosomworth, D. R. Far-Infrared optical properties of  $\text{CaF}_2$ ,  $\text{SrF}_2$ ,  $\text{BaF}_2$ , and  $\text{CdF}_2$ . *Phys. Rev.* **157** (3), 709 (1967).
57. Zhang, J., Li, Y., Cao, K. & Chen, R. Advances in atomic layer deposition. *Nanomanuf. Metrol.* **5** (3), 191–208 (2022).
58. Saleem, M. R., Ali, R., Khan, M. B., Honkanen, S. & Turunen, J. Impact of atomic layer deposition to nanophotonic structures and devices. *Front. Mater.* **1**, 18 (2014).

## Acknowledgements

This work was supported and funded by the Deanship of Scientific Research at Imam Mohammad Ibn Saud Islamic University (IMSIU) (grant number IMSIU-DDRSP2503).

## Author contributions

H. A. E., N. S., and A. M. devised the main ideas and performed numerical simulations. N. S., A. M., H. A. E., A. P., and A. M. A. contributed to the written and revision of the first draft of this manuscript. N. S., A. M., H. A. E., A. P., H. S., M. M. A., M. A. H., W. A. Z., and M. A. A. discussed the results and made the final conclusion, review, editing and revision. All authors contributed to the final manuscript.

## Funding

This work was supported and funded by the Deanship of Scientific Research at Imam Mohammad Ibn Saud Islamic University (IMSIU) (grant number IMSIU-DDRSP2503).

## Declarations

### Competing interests

The authors declare no competing interests.

### Additional information

**Correspondence** and requests for materials should be addressed to H.A.E.

**Reprints and permissions information** is available at [www.nature.com/reprints](http://www.nature.com/reprints).

**Publisher's note** Springer Nature remains neutral with regard to jurisdictional claims in published maps and institutional affiliations.

**Open Access** This article is licensed under a Creative Commons Attribution-NonCommercial-NoDerivatives 4.0 International License, which permits any non-commercial use, sharing, distribution and reproduction in any medium or format, as long as you give appropriate credit to the original author(s) and the source, provide a link to the Creative Commons licence, and indicate if you modified the licensed material. You do not have permission under this licence to share adapted material derived from this article or parts of it. The images or other third party material in this article are included in the article's Creative Commons licence, unless indicated otherwise in a credit line to the material. If material is not included in the article's Creative Commons licence and your intended use is not permitted by statutory regulation or exceeds the permitted use, you will need to obtain permission directly from the copyright holder. To view a copy of this licence, visit <http://creativecommons.org/licenses/by-nc-nd/4.0/>.

© The Author(s) 2025